

Calibrations of SITELLE’s first data release

T. Martin^{1,2*}, L. Drissen^{1,2}

¹*Département de physique, de génie physique et d’optique, Université Laval, 2325, rue de l’université, Québec (Québec), G1V 0A6, Canada*

²*Centre de Recherche en Astrophysique du Québec (CRAQ), Montréal (Québec), H3C 3J7, Canada*

Accepted XXX. Received YYY; in original form ZZZ

ABSTRACT

SITELLE is an imaging Fourier Transform Spectrometer installed at the Canada-France-Hawaii Telescope since July 2015. It delivers spectral cubes covering an $11' \times 11'$ field-of-view with a seeing-limited spatial resolution and a tunable spectral resolution ($R \sim 1\text{--}10\,000$) in selected passbands of the visible band (350–900 nm). We present an accurate picture of the calibration accuracy of SITELLE’s first data release. To this purpose, most of the operations of the reduction pipeline (ORBS) are described in details.

Key words: keyword1 – keyword2 – keyword3

1 INTRODUCTION

SITELLE (Drissen et al. 2010) is an imaging Fourier Transform Spectrometer installed at the Canada-France-Hawaii Telescope (CFHT) since July 2015. It delivers spectral cubes covering an $11' \times 11'$ field-of-view with a seeing-limited spatial resolution and a tunable spectral resolution ($R \sim 1\text{--}10\,000$) in selected passbands of the visible band (350–900 nm). SITELLE is based on an off-axis configuration of the interferometer which gives the opportunity to measure the flux on both output ports instead of one in the classical, on-axis, configuration (see Fig. 1, Grandmont et al. 2012). Two $2k \times 2k$ CCD cameras are attached on the output ports. During an observing scan, the scanning mirror is moved. The optical path difference (OPD) between the two interfering beams is thus gradually changed, step by step, modulating the output intensity according to the spectral energy distribution of the observed source. The images collected at the output are interferometric images which are stacked into two interferometric cubes (one for each output port). For a given pixel in the image, the intensity recorded at each step is thus an interferogram, the Fourier transform of which must be computed to determine the spectrum of the source. More details on the observing process are given in Martin et al. (2016), Drissen et al. (2010) and references therein.

These two interferometric cubes are transformed into one spectral cube with the reduction pipeline ORBS. The details of the operations of the pipeline which have an impact on the calibrations will be discussed in this article. The general

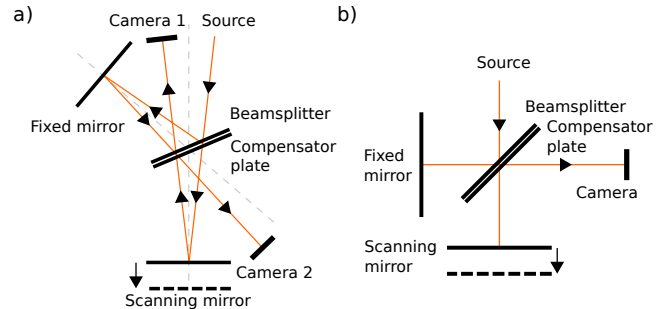


Figure 1. a) Sketch of SITELLE’s interferometer. b) Sketch of a classical Michelson interferometer.

description of the pipeline is given in Martin et al. (2012, 2015) and Martin (2015)¹.

Ideally, the Fourier transform of all the interferograms recorded (around 4 million) would be the only operation required to transform an interferometric cube into a spectral cube of the same dimension. In practice however, a lot of operations on the raw data are actually needed to prepare and merge the interferograms obtained with each camera before being able to compute their spectrum and calibrate the obtained spectral cube. The main focus of this article is to give an accurate picture of the calibration accuracy of SITELLE’s first data release. Note that this calibration will certainly be improved with the next data releases. Some of them are described in Martin et al. (in preparation). Section 2 gives an overview of the reduction pipeline. In section 3 we describe in details the phase correction process which can have a ma-

* E-mail: thomas.martin.1@ulaval.ca

¹ ORBS source code can be found at <https://sourceforge.net/projects/orb-orbs/>.

for impact on the flux and the wavelength calibrations. Flux calibration, wavelength calibration and astrometric calibration are considered respectively in sections 4, 5 and 6.

Note that some of the most important results of this paper have already been presented in a conference proceedings (Martin & Drissen 2016) but in a much less detailed fashion.

2 REDUCTION PROCESS

Data calibration is the last step of the reduction pipeline. But each step of the reduction has an impact on the quality of the calibration, and especially the flux calibration. There has been some changes since the description of the pipeline given in Martin et al. (2012, 2015); Martin (2015). We present here the up-to-date version of the general processing pipeline:

(i) Calibration of the CCD images: bias is computed from the overscan columns and subtracted, flat-field illumination errors are corrected. No dark is subtracted because the dark current is very low ($< 2 e^-/hr^2$) and in this case dark subtraction would enhance the noise in the images without having a significant impact on the quality of the flux calibration (see section 4.2.1). Images are also realigned to compensate for guiding errors

(ii) Alignment of the cubes. There is a slight optical misalignment between the cameras. As this alignment is expected to change when the cameras are removed, the stars detected in the field-of-view are used to compute the alignment parameters for each cube.

(iii) Combination of the cubes. The two interferometric cubes are combined to enhance the SNR, correct for transmission variations of the sky during the observation and remove the unmodulated background light (see section 4.2.2).

(iv) Phase computation of the combined cube (see section 3).

(v) Transformation of the combined cube to a spectral cube. The transformation is based on a discrete Fourier transform (DFT) of each interferogram. The phase information obtained from the phase cube is used at this point.

(vi) Calibration of the spectral cube (see sections 4, 5 and 6).

The impact of these reduction steps on the final calibration will be discussed throughout the paper.

3 PHASE CORRECTION

Phase correction is done when the combined interferometric cube is transformed to a spectral cube via a discrete Fourier transform operation. It has an impact on flux and wavelength calibrations (see e.g. Bell 1972). A bad phase correction will result in a deformation of the instrument line shape (ILS) which leads to flux and wavelength errors.

² See the specification of the e2v's back-illuminated 2kx2k scientific CCD sensor CCD230-42 at <http://www.e2v.com/resources/account/download-datasheet/3828>

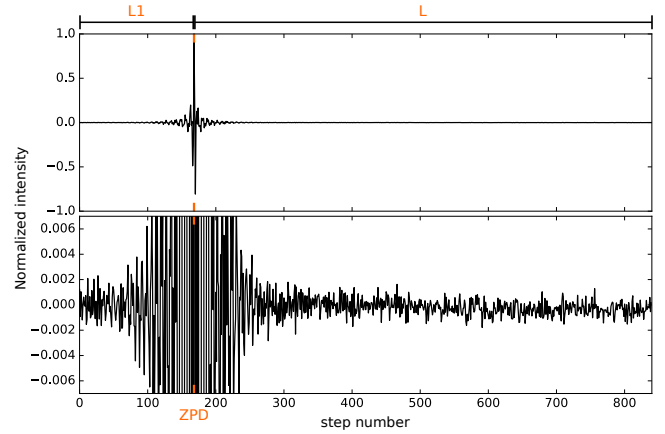


Figure 2. Example of a typical continuum source interferogram obtained with SITELE. It has been recorded near the center of M31 in the SN3 filter (courtesy of Anne-Laure Melchior). The top panel shows the full interferogram and the bottom panel shows a zoomed version. The ZPD (step 168, indicated with an orange tick) is positioned at the highest measured intensity of the interferogram. The maximum OPD attained on the left side is L_1 and L on the right side (see equations 8 and 9).

If the source has a spectral distribution $S(\sigma)$, the intensity measured at an optical path difference (OPD) x will be (Sakai et al. 1968):

$$I(x) = \int_{-\infty}^{+\infty} S(\sigma) e^{i\phi(\sigma)} e^{2i\pi\sigma x} d\sigma \quad (1)$$

where $\phi(\sigma)$ is a phase error which may arise from dispersive effects in the optics of the interferometer and a non perfect sampling. Note that, when both the fixed and the moving mirrors are at the same distance from the beamsplitter, the OPD x is equal to 0 (this position is called the Zero Path Difference, ZPD); in the absence of phase error ($\phi(\sigma) = 0$), the intensity measured is equal to the total intensity of the source. Which means that, at ZPD, an interferogram is at its maximum intensity (see figure 2).

The Fourier transform of a non-corrected interferogram is therefore

$$\hat{I}(\sigma) = S(\sigma) e^{i\phi(\sigma)} = \int_{-\infty}^{+\infty} I(x) e^{-2i\pi\sigma x} dx \quad (2)$$

In the absence of phase errors, the spectrum corresponds to the real part of the Fourier transform. However, any uncorrected phase error will translate into an error in the calculated spectrum (see Figure 3). A first approach consists in computing the power spectrum to remove the phase error

$$P(\sigma) = |\hat{I}(\sigma)|^2 = S(\sigma)^2 e^{i\phi(\sigma)} e^{-i\phi(\sigma)} = S(\sigma)^2. \quad (3)$$

However, the ILS is modified, the spectral resolution is degraded and the noise properties of the spectrum are much different as its distribution is squared. A better approach to recover the real spectrum is therefore to compute the phase and remove it from the Fourier transform

$$S(\sigma) = \text{Re} \left(\hat{I}(\sigma) e^{-i\phi(\sigma)} \right). \quad (4)$$

The whole challenge of phase correction is thus to recover the phase $\phi(\sigma)$, which is different from one interferogram to the other, with the highest precision possible so that the quality of the spectrum is ideally not affected by this operation.

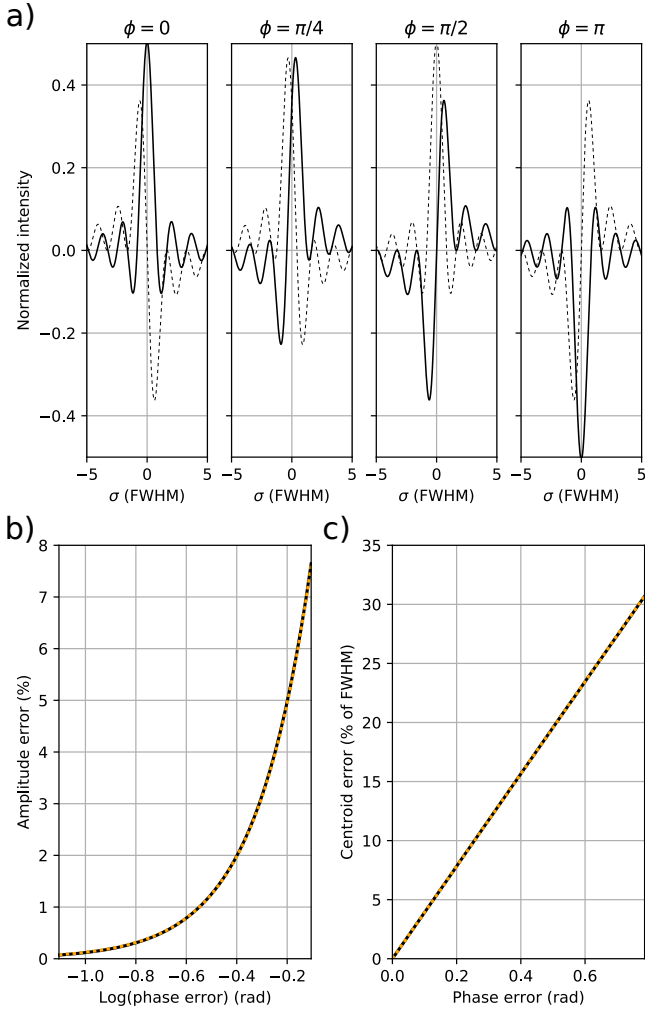


Figure 3. *a)* Effect of a constant phase error on the instrument line shape. The real part is drawn in solid black and the imaginary part is dotted. The wavenumber σ is given in units of the line's FWHM. *b)* Effect of constant phase error on the amplitude of the line. The black line represents the numerical simulation and the dotted orange line represents the curve given in equation 18. Note that phase error (given in log) goes from $0.1\pi/4$ to $\pi/4$. *c)* Effect of constant phase error on the measured position in percentage of the line FWHM.

3.1 Determination of the phase

The discrete Fourier transform of an interferogram of N samples is

$$\hat{I}(\sigma) = \sum_{n=0}^N I(x_n) \exp(-2i\pi\sigma x_n) = \hat{I}_{\text{Re}}(\sigma) + i\hat{I}_{\text{Im}}(\sigma). \quad (5)$$

The phase $\phi(\sigma)$ of the complex spectrum is simply

$$\phi(\sigma) = \tan^{-1} \left(\frac{\hat{I}_{\text{Im}}(\sigma)}{\hat{I}_{\text{Re}}(\sigma)} \right). \quad (6)$$

If $\phi(\sigma)$ is not 0, the corrected spectrum is calculated by removing the phase before taking the real part (see equation 4).

In the absence of prior informations, the phase is an unknown function of the wavenumber and can be different from one pixel to another (i.e. different for each interferogram of

the cube). It is considered as a slowly varying function which, when computed from equation 6, contains some noise that must be removed before it is used to correct the spectrum. A polynomial model is thus fitted to obtain a noiseless phase which can be interpolated between the samples calculated with the DFT (Sakai et al. 1968).

$$\phi(\sigma) \equiv p_0 + p_1\sigma + p_2\sigma^2 + \dots \quad (7)$$

If the interferogram is asymmetric, only the symmetric part around the ZPD is used to compute the phase. Ideally, one would try to obtain a symmetric interferogram to maximize the quality of the calculated phase. But, on the other hand, as the resolution depends on the maximum path difference attained with respect to the ZPD (see equation 9), the samples recorded symmetrically contribute to the SNR only. Therefore, in order to maximize the attained resolution for a given exposure time, SITELLE's interferograms are not recorded symmetrically. The shortest side of OPD, L_1 , before reaching the ZPD, extends to 25% of the longest side of OPD L (see Figure 2). As the phase is computed with the samples that are distributed symmetrically around the ZPD (e.g. Bell 1972), the resolution of the phase vector, R_ϕ , depends on L_1 (see e.g. Martin et al. 2016 for more details on the calculation of the resolution):

$$R_\phi = \frac{2\sigma L_1}{1.20671}, \quad (8)$$

while the resolution of the spectrum is 4 times higher,

$$R = \frac{2\sigma L}{1.20671}. \quad (9)$$

Ideally, once the phase at each pixel is fitted with a high order polynomial, a 3D phase cube is obtained that can be used directly to correct the spectral cube, spectrum by spectrum, with no further considerations. Each order of the fitted polynomial is mapped pixel-by-pixel and these maps contain enough information to reproduce the phase cube. In fact, the SNR of the phase vector is rarely high enough or not homogeneous enough in the whole passband that such a straight approach can be used. Indeed, from equation 6, we can see that the precision of the phase measured in a given channel depends on the SNR of the real part and the imaginary part of the spectrum. As the noise is equally distributed over all the channels, the precision on the phase is thus directly proportional to the spectral energy distribution of the observed source. An emission-line spectrum, typical of an H II region, will therefore generate a reliable phase information only at the wavelength of the lines, while a continuum source (like a star, a galaxy or the earth atmosphere) will be much better at providing a reliable phase in the whole observed passband (Learner et al. 1995).

Therefore, the quality of the measured phase value will be different from one channel to the other and also from one spectrum to the other. The spatial correlation of the pixels, along with some modelling, must be used to enhance the quality of the computed phase vectors. As the model used to fit the phase of all the spectra is a polynomial, each order of the polynomial can be mapped and each map can be fitted with a model. Having models which depend on a small number of meaningful parameters, such as optical and mechanical parameters, thus appears fundamental.

3.1.1 First order

The first order of the polynomial, p_1 , reflects the fact that the ZPD is not properly sampled, i.e. the OPD, measured on-axis, of the sample nearest to the real ZPD is $\epsilon_x \neq 0$ (see e.g. Davis et al. 2001). The real OPD at a given step is

$$x = n\delta_x + \epsilon_x, \quad (10)$$

with δ_x the step size and n the step index (with respect to the ZPD sample where $n = 0$). The phase value in equation 1 becomes

$$\phi_1(\sigma) = 2\pi\sigma\epsilon_x. \quad (11)$$

This relation is not complete since we know from equation 29 that the OPD depends on the incident angle and so does the sampling shift $\epsilon_{x,\theta}$

$$\epsilon_{x,\theta} = \epsilon_x \cos(\theta). \quad (12)$$

We can now write the first order phase created by this sampling shift at any incident angle

$$\phi_1(\sigma) = p_1(\theta) = 2\pi\sigma\epsilon_{x,\theta} = 2\pi\sigma\epsilon_x \cos(\theta). \quad (13)$$

As the incident angle can be directly deduced from the observation of a laser source illuminating an integrating sphere (see section 5 and equation 36), only one parameter, ϵ_x , is necessary to fit the map derived from the independent fit of the phase of all the spectra of the cube.

3.1.2 Orders larger than 1

All phase orders larger than 1 are considered to reflect some kind of dispersive effect. For example, if the beamsplitter and the compensator plate do not have the exact same thickness (see Fig. 1), the phase becomes (see e.g. Davis et al. 2001)

$$\phi_{\geq 2}(\sigma) = 2\pi\sigma r(\sigma)d(\theta). \quad (14)$$

with $d(\theta)$ the thickness difference, which may change with θ , and $r(\sigma)$ the refractive index. For this data release we have considered that $d(\theta)$ was constant enough that the higher order of the phase could be approximated by the same function everywhere in the cube. We have checked that the error made with this approximation was smaller than 1% in relative flux error and that the relative wavelength calibration error was below 5% of the FWHM, i.e. the difference between the median high order phase used for phase correction and the high order phase measured at any point of the cube is smaller than 0.1 rad (see figure 4).

3.1.3 Zeroth order of the phase

In the ideal case, the phase shift between the two beams interfering at the beamsplitter is $2\pi\sigma x + \pi$ (Bell 1972, p.113). We have already seen that the OPD x can be subject to a shift plus additional dispersive effects that explain non-zero polynomial coefficients at orders larger than 0. The constant term π is also subject to change. For example, absorption in the beamsplitter will change the constant value (Bell 1972, p.125) and therefore the constant phase

$$\phi_0(\sigma) = \pi + 2 \arctan \frac{2K(\sigma)}{r(\sigma)^2 + K(\sigma)^2 - 1} \quad (15)$$

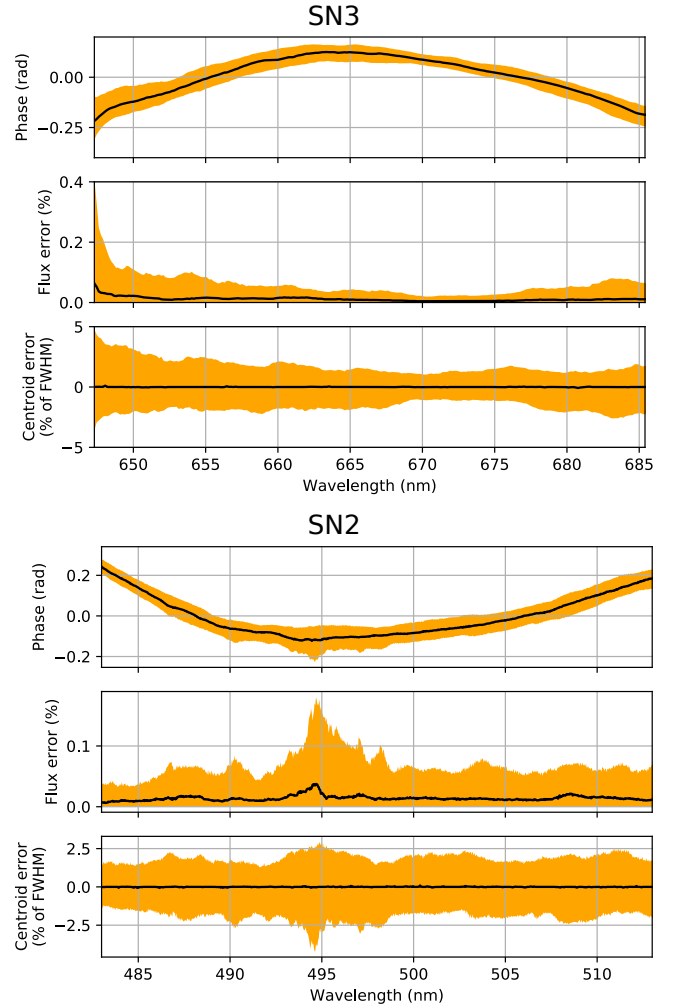


Figure 4. Median high order phase in the SN2 and SN3 filters. *Top quadrant:* Median phase computed along the wavenumber axis. The values of the phase between the 16th and 84th percentiles are represented as an orange surface. *Center and bottom quadrants:* Distribution of the flux error (center quadrant) and line centroid error (bottom quadrant) made by using the median phase instead of a phase computed for each pixel of the cube (see equations 18 and 19). The median error is in black and the 16th and 84th percentile of the error distribution is represented as an orange surface.

with $r(\sigma)$ and $K(\sigma)$ respectively the refractive and absorption indexes.

The effect of an error on the constant term can be studied by considering an erroneous phase $\phi(\sigma) = \delta p_0$ applied to a perfect interferogram. Equation 4 can then be written

$$S(\sigma) = \text{Re} \left(\hat{I}(\sigma) e^{-i\delta p_0} \right) \quad (16)$$

$$= \hat{I}_{\text{Re}}(\sigma) \cos(\delta p_0) + \hat{I}_{\text{Im}}(\sigma) \sin(\delta p_0) \quad (17)$$

This will result in mixing the real and imaginary parts of the spectrum (see figure 3). The error made on the line amplitude is then:

$$\Delta_{\text{Flux}} [\%] = 100 \times \left[1 - \cos \left(\frac{\delta p_0}{2} \right) \right]. \quad (18)$$

The error made on the line centroid is, in percentage of the

FWHM,

$$\Delta_{\text{Centroid}} [\%] = 39.1 \times \delta p_0. \quad (19)$$

Note that these relations have been empirically calculated from a numerical simulation. The results of the numerical simulation are plotted in Figure 3. As the phase is a slowly varying function of the wavelength, these relations can be used to compute the effect of a phase error no larger than $\pi/4$ at a given wavelength (the phase error is then considered as locally constant). As one can see on Figure 3, when the phase error is larger than $\pi/4$ the negative lobe becomes important and even the notion of “line” starts to be doubtful.

3.1.4 Phase correction method

When the field is covered with continuum sources (earth atmosphere, galaxies, low surface brightness diffuse gas) the two first orders of the phase can be determined without the need for external calibration data. In most of the cubes (galaxy clusters, star clusters, extra-galactic objects in general), phase computation relies on the sky background which, in most regions, is bright enough with respect to the emission-lines of the observed astrophysical sources that a reliable phase measurement can be obtained in all the observed band (Learner et al. 1995). In this case a not too noisy phase vector can be computed at each pixel of the cube, thus providing a phase cube. The high-order phase (orders larger than 1) which has been computed from a high-resolution scan of a white-light source observed through an integrating sphere (see section 3.1.2) is subtracted and a first degree polynomial can be fitted on every phase vector of the cube. The output from the fit are a map of order 0 which can be fitted with the model described in section 3.1.3 (see Figure 5) and the coefficient of order 1³ (see section 3.1.1). A precise phase vector can then be reconstructed for each pixel and used for phase correction.

3.2 Instrument line shape

The ideal instrument line shape (ILS) of a phase corrected Fourier transform spectrum is a sinc. Any error in the phase correction will result in a deformation of the ILS (see Figure 3). Non-symmetric modulation efficiency loss with the OPD (documented in Baril et al. 2016) can also generate an asymmetric ILS that will eventually be the source of wavelength and flux errors. The ILS is very well described by the theoretical model used to fit the emission lines described in Martin et al. (2016) despite a small modeling error that can be detected by fitting high SNR spectra. This error is located near the right lobe of the sinc and its amplitude, with respect to the central lobe, is around 1% (see Figure 6). If this error was produced by a phase error, a negative residual on the right lobe of the sinc would be compensated by a positive residual on the left lobe, which is not the case.

³ In some earlier versions of the code, a map of the first order was computed and fitted with a spline model. In all cases the error made on its estimate was negligible with respect to the order 0.

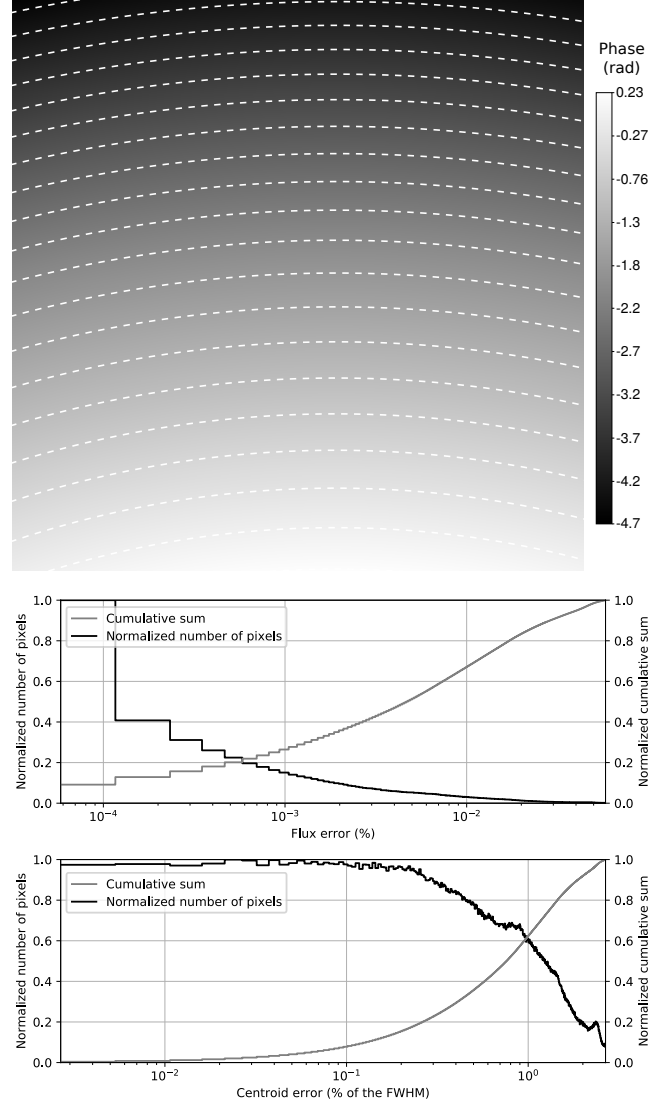


Figure 5. *Top:* Typical map of the order 0 phase coefficient, contours have been over-plotted. (from a scan of M31 in the SN3 filter, courtesy of Anne-Laure Melchior). *Center and bottom:* Histograms of the residual between the phase map and the fitted model in terms of flux error (center, equation 18) and line centroid error (bottom, equation 19). The cumulative sum corresponding to the histogram is also shown. Both curves are normalized.

4 FLUX CALIBRATION

4.1 Flux calibration method

Flux calibration is based on the measurement of the spectrum of a spectrophotometric standard star in each filter. The obtained spectrum is used to correct for the wavelength dependent transmission of the instrument and the telescope. A set of images of a standard star is also obtained at least once for each scan which provides a measurement of the mean sky transmission in the filter band during the scan.

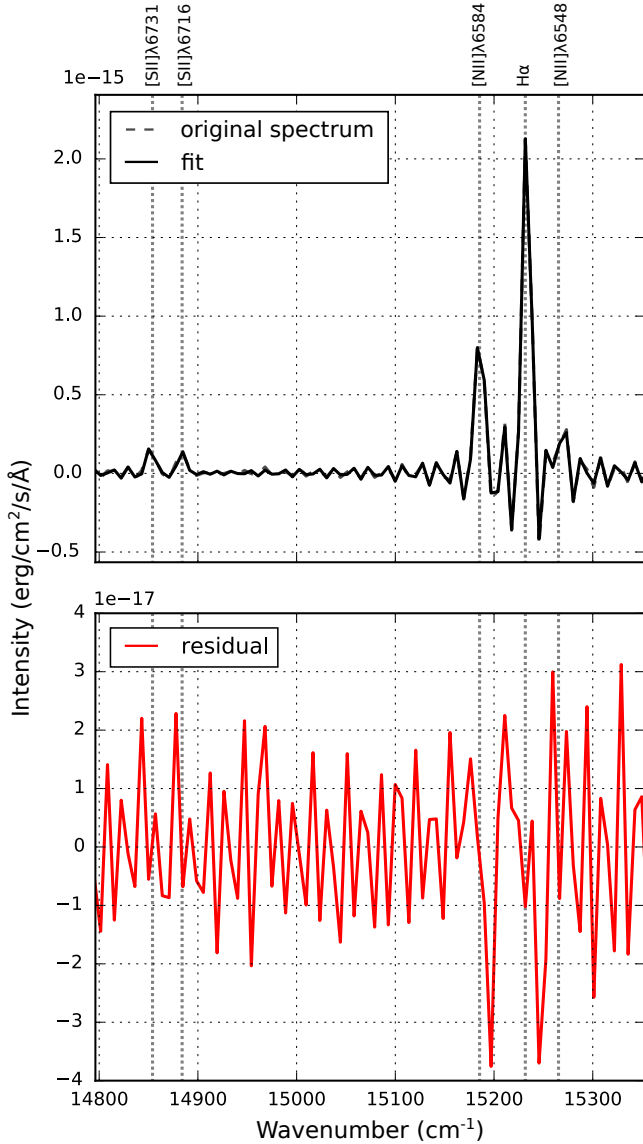


Figure 6. Example of a fit realized with ORCS (Martin et al. 2015) on a spectrum of a bright region of an HII region in the red SN3 filter. The model used is the convolution of a Gaussian emission line and a sinc ILS (Martin et al. 2016). A modeling error is clearly visible near the right lobe of the emission lines.

4.1.1 Absolute flux calibration

Absolute flux calibration consists in relating the real flux (in $\text{erg cm}^{-2} \text{s}^{-1}$) to a measured flux of 1 count per second. As the Fourier transform conserves the energy from the interferogram to the spectrum (in the ideal case, when the modulation efficiency is 1), the flux calibration calculated for an interferogram holds for the calculated spectrum. It can therefore be made by taking a simple image of a standard star as one would do to calibrate typical imager data.

The number N of counts per second measured at one of the detectors from a star of flux density F_* (in

Table 1. Typical values of the transmission terms calculated for each SITELLE’s filters. Telescope transmission is based on the values provided by the CFHT. The atmospheric transmission at one airmass comes from Buton et al. (2012). The optics transmission have been provided by ABB Incorporated. Note that there are some differences with the previous estimations reported in the figure 9 of Grandmont et al. (2012).

Filter	SN1	C1	SN2	C2	SN3
ME	0.6	0.7	0.8	0.8	0.8
$T_{\text{atm.}}$	0.73	0.83	0.89	0.91	0.95
$T_{\text{tel.}}$	<0.92	0.92	0.92	0.91	0.90
$T_{\text{opt.}}$	0.67	0.69	0.67	0.69	0.66
T_{filter}	0.94	0.97	0.97	0.95	0.97
QE	0.69	0.90	0.88	0.90	0.92

$\text{erg cm}^{-2} \text{s}^{-1} \text{Å}^{-1}$) can be written

$$N = 0.5 \int_{-\infty}^{+\infty} \frac{\lambda F_*(\lambda)}{hc} T_{\text{atm.}}(\lambda) S_{\text{prim.}}(\lambda) T_{\text{tel.}}(\lambda) T_{\text{opt.}}(\lambda) \times T_{\text{filter}}(\lambda) G QE(\lambda) d\lambda, \quad (20)$$

where h is the Planck constant, c the speed of light, $T_{\text{atm.}}$, $T_{\text{tel.}}$, $T_{\text{opt.}}$ and T_{filter} are respectively the transmission coefficient of the atmosphere, the telescope optics, SITELLE’s optics and the filter; G is the gain and QE the quantum efficiency of the CCD. The factor 0.5 comes from the fact that, because of the beamsplitter, only half the input light is recorded by one of the detectors. Equation 20 can be used to calculate the number of counts measured for a star with a known flux density. Typical values of the different terms for each filter are given in Table 1.

When we calibrate our data with an image the number of counts per second is a measured quantity that must be related to the intensity of the star in the filter passband (in $\text{erg cm}^{-2} \text{s}^{-1}$).

$$\bar{F} = \int_{-\infty}^{+\infty} F_*(\lambda) \tilde{T}_{\text{filter}}(\lambda) d\lambda \simeq \int_{\lambda_{\text{min}}}^{\lambda_{\text{max}}} F_*(\lambda) d\lambda, \quad (21)$$

where $\tilde{T}_{\text{filter}}$ is the normalized filter function; λ_{min} and λ_{max} are the minimum and maximum wavelength of the equivalent ideal filter bandpass.

Even if SITELLE’s modulation efficiency is very high in the whole visible band, it is never equal to 1 (Drissen et al. 2010) so that the calibration coefficient α by which a spectrum in $\text{ADU s}^{-1} \text{Å}^{-1}$ must be multiplied is

$$\alpha = \frac{N}{\bar{F} \times ME}, \quad (22)$$

where ME , the modulation efficiency, is defined as the ratio of the amplitude of the modulated signal over the amplitude of the input signal.

$$ME = \frac{\text{Amplitude of the modulated signal}}{\text{Amplitude of the input signal}}. \quad (23)$$

If the signal is monochromatic, it can be measured everywhere. In all other cases, its reference value must be measured at the ZPD. The modulation efficiency is very sensitive to the quality of the optics (reflection index and surface quality of the mirrors and the beamsplitter) and their alignment during the exposure (e.g. Drissen et al. 2010; Maillard et al. 2013; Baril et al. 2016).

A rough measurement of the modulation efficiency at

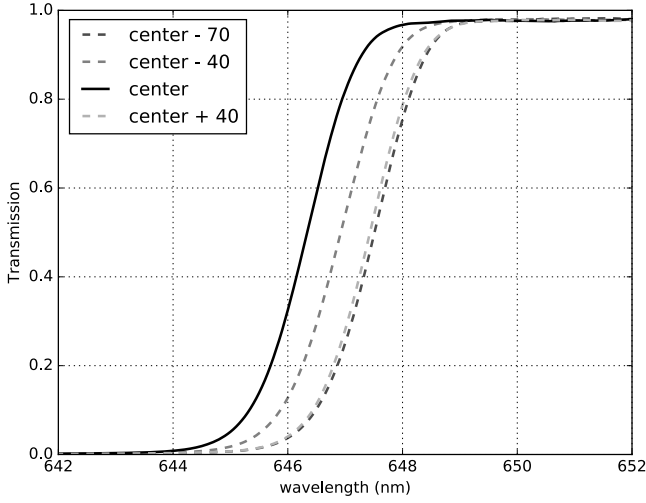


Figure 7. Edge of the SN3 filter at different positions in the field of view.

ZPD has been made based on simulated values by ABB and cubes of laser sources observed at different wavelengths during the testings of the instrument before it was shipped to the CFHT (see Table 1). The precision on this measurement is around 5% and is likely to vary from one scan to another. When the amount of stray light is negligible, the modulation efficiency is the ratio between the energy of the input interferogram and the computed spectrum. As a certain amount of stray light has been measured in SITELLE's interferometric images, a robust algorithm still has to be developed in order to obtain a much more precise measurement of the ME that would ideally reflect the real mean modulation efficiency of each observation.

Note that airmass is not taken into account in the atmospheric transmission coefficient. As its value is different for the standard star and the science target we must correct the calibration coefficient by the difference of transmission due to the airmass. However, this correction has not been considered for this data release as its impact is negligible with respect to the other sources of uncertainty (see section 4.2).

4.1.2 Wavelength dependent flux calibration

4.1.2.1 Filter transmission As the filter passband is not the same everywhere in the field (see Figure 7), filter correction requires the determination of a 3D transmission function which was not known precisely enough for the data release 1. Therefore, no filter correction has been done. Note that the edges of the filters are quite steep and the peak-to-peak difference in the passband is not higher than 4% and generally smaller than 2% (see Figure 8).

4.1.2.2 Instrumental transmission Following equation 20, we see that a lot of optical media with different transmission functions are contributing to the whole instrument transmission (here the concept of “instrument” is equivalent to the combination of SITELLE, the telescope and the atmosphere). The knowledge of the exact impact of each parameter of this function is unimportant since we can determine the instrumental transmission $T_{\text{instrument}}$ from

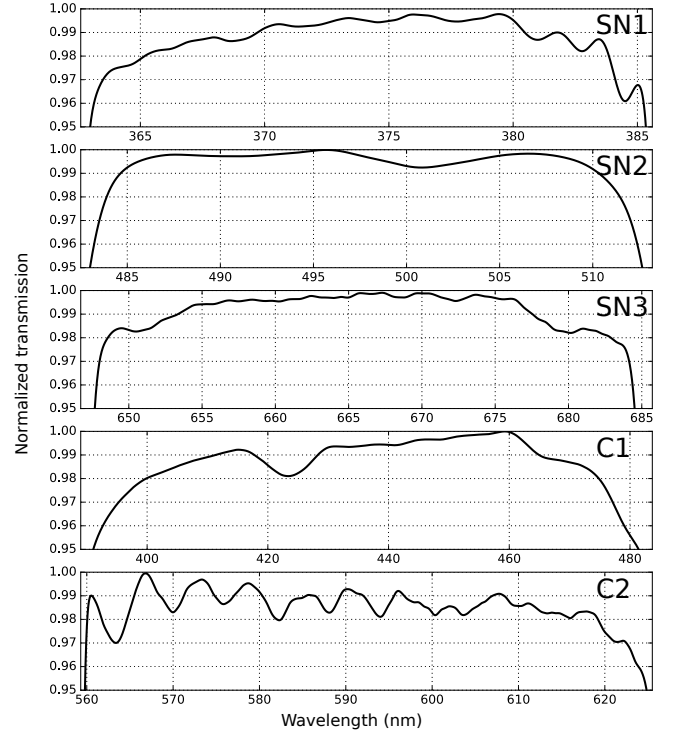


Figure 8. Normalized SITELLE's filter transmission curves. Note that filters SN2 and C1 have been scanned at a lower resolution and may seem falsely smoother than the others.

the measured spectrum of a standard star. Indeed, we can write

$$T_{\text{instrument}}(\lambda) = T_{\text{atm.}}(\lambda) T_{\text{tel.}}(\lambda) T_{\text{opt.}}(\lambda) \times T_{\text{filter}}(\lambda) G Q E(\lambda), \quad (24)$$

and,

$$T_{\text{instrument}}(\lambda) = \frac{\alpha S_{\star}(\lambda)}{F_{\star}(\lambda)}, \quad (25)$$

where S_{\star} is the measured spectrum in $\text{ADU s}^{-1} \text{\AA}^{-1}$ and α is the calibration coefficient computed from standard images (see equation 22). The calibration function by which a spectrum must be multiplied is the inverse of the instrumental transmission. The flux calibration functions computed for the filters SN1, SN2 and SN3 are shown on Figure 9 along with a model based on our knowledge of the different transmission functions considered in equation 24. We can see serious differences between them that must be due to our poor knowledge of the transmission function of the telescope mirrors (especially in the blue part of the SN1 filter). It is also clear that the important noise on the measured standard spectrum makes the uncertainty on the relative flux calibration around 5%. Noise is very difficult to reduce when observing bright stars because of the detectors saturation. The only method that would seriously enhance the precision of the flux calibration function would be to observe at the same time a very high number of secondary calibration sources like star clusters for which standard spectra would have been obtained independently.

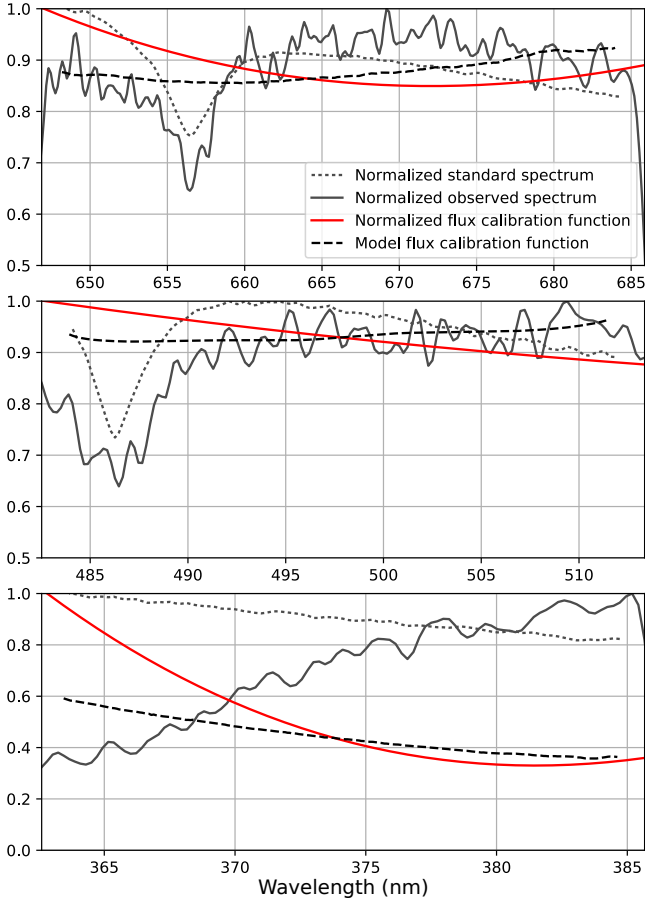


Figure 9. Normalized SITELLE’s flux calibration functions. The observed spectrum of the standard star and the standard spectrum are shown. The model calibration function based on our knowledge of the different transmission functions considered in equation 24 is also shown. This model is not used for the calibration.

4.2 Influence of the reduction steps on the flux calibration

Flux calibration is certainly the most sensitive to the quality of each reduction step. We are going to analyze the relative contribution of each reduction step on its precision.

4.2.1 Image correction and alignment

As with any imager, the number of counts recorded in each pixel must first be corrected for electronic and thermal biases, coming from the detector, as well as differences in the illumination pattern due to the whole optical system comprising the telescope and the instrument optics. This corrected flux must also be conserved through the alignment steps which are all based on linear interpolation. All those first steps have an influence on the homogeneity of the measured flux in each image taken independently.

4.2.1.1 Flat-field Flat-field correction is the most important contributor in terms of relative flux calibration errors. Flat-field images are obtained by observing the sky at twilight through the same filter used to observe the science

data. Five images are taken at the beginning of each night and combined to make a master flat-field image which is used to correct the illumination pattern of the science images. The combination is an implementation of the averaged sigma-clipping algorithm of the task `imcombine` of the package `stdas` of the IRAF pipeline (Doug 1993). In the worst cases a gradient in the sky level of up to 5% has been seen in the corrected images. The maximum difference is seen in the corners of the image.

4.2.1.2 Alignment Once the alignment parameters are found by measuring the positions of the stars in the field of view with a Gaussian profile fitting algorithm, images are geometrically transformed with a classic linear interpolation algorithm. Even if linear interpolation will certainly modify the shape of a star and therefore cannot guarantee flux conservation, a simulation of this effect shows that the flux is perfectly well conserved for stars if aperture photometry is used, i.e. the total number of counts in a circular aperture around the star is conserved. This result is obvious since the interpolation of any signal will conserve the value of the integral of the signal. We have therefore not detected any error on the flux measurement larger than the numerical error with aperture photometry. But profile fitting will give a worse estimate of the flux since the overall shape is modified. For example, the peak value of the transformed point spread function (PSF) is around 0.5 the peak value of the real PSF. If a fitting procedure is used (in the idealized case of a Gaussian PSF), the median error made on the flux measurement is around -2% (flux is always underestimated) and the largest error is always smaller than -5% (over 5000 randomized tries).

4.2.2 Cube combination

During the combination step it is possible to correct for temporal variations of the atmospheric transmission. Remember that the cubes are complementary by definition, the light that does not go through one of the output ports must go through the other. Combining both cubes has therefore two advantages. (1) It provides two times more photons, which enhances the signal-to-noise ratio (SNR) by a factor of $\sqrt{2}$. (2) Given the fact that all the input light ends on both output ports it is possible to follow the flux variation of the input light. With the assumption that the source is not variable and that the overall transmission remains stable during the observation, the variation of the sum of the flux measured on both ports gives a robust estimate of the variation of the mean sky transmission in the observed passband (atmospheric extinction and airmass).

A first order combination equation of the two interferograms of the same source is

$$I(t) = \frac{I_1(t) - I_2(t)}{I_1(t) + I_2(t)}, \quad (26)$$

I_1 and I_2 being the interferograms recorded in camera 1 and camera 2 respectively (Davis et al. 2001; Martin et al. 2012); t is the time when each sample is recorded. Because the interferograms measured on each arm are complementary (i.e. all the incoming flux is separated between each arm), $I_1 - I_2$ represent the modulated part of the interferogram while $I_1 + I_2$

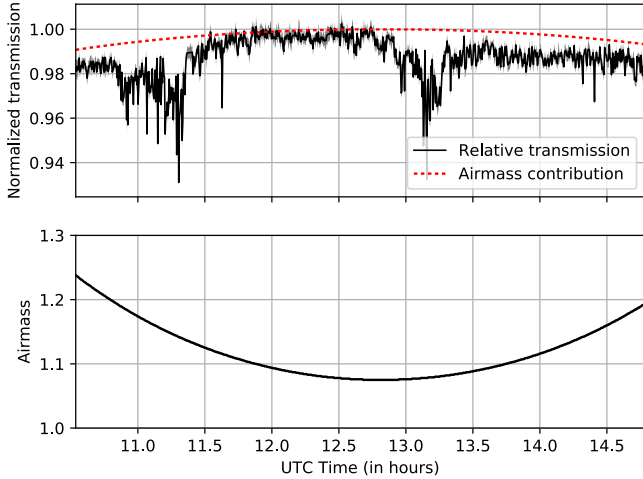


Figure 10. *Top:* Atmospheric transmission function during the acquisition of the M31 cube in the SN3 filter observed on August 24, 2016 (courtesy of Anne-Laure Melchior, see Martin et al. 2017 in preparation). The computed transmission is normalized to its 99th percentile. The grey surface represents the uncertainty. The airmass contribution to the atmospheric transmission is plotted in dotted red. It as been computed with a mean value of the extinction over the Mauna Kea at the $H\alpha$ wavelength of $6.2 \cdot 10^{-2}$ mag/am quoted from Buton et al. (2012). *Bottom:* Estimated airmass of the observed target.

is the intensity at the input of the interferometer. The relative variation of the atmospheric transparency is thus corrected by the denominator. As $I_1 + I_2$ must be the same for all the pixels of the cube we can use the stars to compute an atmospheric transmission function $T_{\text{atm.}}(t) = I_1(t) + I_2(t)$ for all the interferograms. We use the stars to compute the transmission because the measure of their flux is much less sensitive to scattered light. A typical atmospheric transmission function is shown in Figure 10. Equation 26 can thus be rewritten

$$I(t) = \frac{I_1(t) - I_2(t)}{T_{\text{atm.}}(t)}, \quad (27)$$

There are two underlying assumptions in this equation:

- The detectors are sufficiently similar that the quantum efficiency (QE) is the same at all wavelengths.
- Since the subtraction at the numerator will remove any amount of stray light equally found in both cameras, the difference in the amount of stray light ending in both cameras must be negligible.

While these two assumptions could not hold in the case of its predecessor SpIOMM (Grandmont 2003; Bernier 2006), they are considered true in the case of SITELLE.

4.2.3 Phase correction

Remember that the phase vector used to correct a given spectrum is computed from two polynomial coefficients: order 0, which is mapped and order 1, which reduces to one number for the whole cube and the higher order phase, which is a function of the wavenumber calculated from a continuum calibration source observed once by run (a SITELLE

run never lasts more than 10 nights). The spectrum attached to pixel k will be corrected with a phase vector $\phi(k, \sigma)$:

$$\phi(k, \sigma) = p_0(k) + \sigma p_1 + \phi_{\geq 2}(\sigma) \quad (28)$$

The error (in percentage) on the measure of the flux resulting from an error in the determination of the phase at any given wavenumber can be computed from equation 18. If we assume that the order 0 phase map is a slowly varying function of the position in the field-of-view, i.e. there is no discontinuity between one pixel and its neighbours (see Figure 5), then a model can be fitted and the residual which will contain noise and modelling errors will provide a conservative estimate of the error made (i.e. noise is considered negligible, which is certainly not true). Even in this case, the flux error based on this residual is always much smaller than 1 percent and appears negligible when compared to the flat field uncertainty.

4.3 Assessment of the uncertainty

4.3.1 Uncertainty on the absolute flux calibration

From the analysis conducted in this section we conclude that there are two major sources of uncertainty on the absolute flux calibration: the modulation efficiency measurement and the determination of the mean atmospheric transmission loss from standard star images. Potential phase correction errors seem completely negligible at this point.

We have checked the accuracy of the calibration against various references: independent point-like sources (galaxies at $z \sim 0.3$ in the HETDEX Field, the compact planetary nebula M1-71) and the integrated spectrum of a galaxy covering the whole field of view in three different filters (NGC 628, see Figure 11). All the results are reported in Table 2. There is an obvious general bias around -5% which must come from the rough knowledge of the modulation efficiency. A better estimate of the modulation efficiency could be derived from the ratio of the total spectral energy present in the output spectra and the total energy deposited by the photons in the input interferograms. It will be corrected in a future release of the reduction code. We also must mention that a modulation efficiency loss of 10% has been measured during the observation of the SN3 cube of M31 (see Martin et al. in preparation). In general the modulation efficiency does not vary much from one observation to another which implies that, even if the estimate is biased, its precision is better than 5%. However, as for the first data release, a conservative evaluation of the uncertainty on the modulation efficiency should be between -10% and 0%. Laser frames are obtained at the beginning and the end of each scan which should permit to calculate the modulation efficiency loss in future releases.

As for the measure of the mean atmospheric transmission during the scan, we have also observed that, in rare cases, the standard star images were not taken right before or after the scan and sometimes a night later. In these cases, the measurement is completely unreliable and should not be trusted. The chosen method also suffers from the fact that the transmission can vary by more than 10% on a time scale of a few minutes, which means that the atmospheric transmission measured right after the scan sequence may not reflect precisely even the last minutes of the observation.

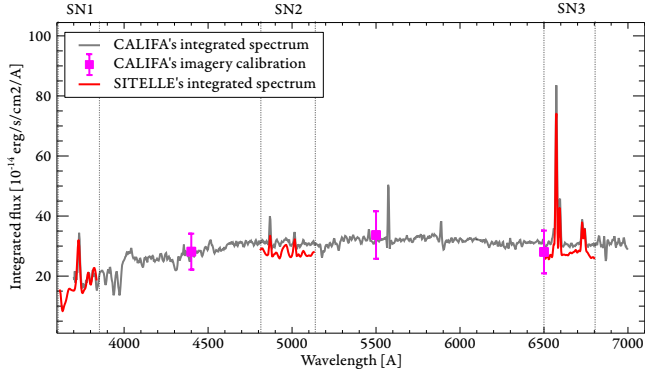


Figure 11. Integrated spectrum of NGC 628 obtained with SITELLE in three filters (SN1, SN2 and SN3) superimposed on the integrated spectra obtained with PPAK (Sanchez et al. 2010; Kelz et al. 2006). SITELLE's spectra have been convoluted to respect PPAK's low resolution. A correction factor of 0.65 has been applied to consider PPAK's filling factor. The photometric calibration points used to calibrate PPAK spectrum are shown in purple along with their uncertainty. Part of the figure has been taken from Sanchez et al. (2010)

An evaluation of the precision of the flux calibration, taking the 5% bias into account, is thus generally between -10% and 0% if we consider the calibration checks reported in Table 2. But a more conservative estimation should be considered to lie between -15% and 5%.

In a general case we recommend that the absolute flux calibration be checked against external data.

4.3.2 Uncertainty on the relative flux calibration

The pixel-to-pixel precision of the flux calibration has been checked by comparing the $H\alpha$ map of the planetary nebula M 57 obtained with SITELLE and the map obtained through the F656N filter of the Hubble Space Telescope (O'Dell et al. 2013). After a careful alignment and convolution of the HST map to respect SITELLE's pixel scale, an histogram of the flux ratio has been computed (see Figure 12). We can see that the error is smaller than 1.5% and the standard deviation of the ratios is smaller than 1.6%. Note that the object covers only a small part of the field of view (around 1×1 arcminute) so that large gradient cannot be detected. Another example of the pixel-to-pixel flatness of the flux calibration is given in Martin et al. (in preparation) for the calibration of M 31. Up to now, no overall gradient has been detected and the relative flux calibration seems better than 3%.

5 WAVELENGTH CALIBRATION

Recording an interferometric image implies to measure the flux at different angles θ with respect to the interferometer axis where $\theta = 0$. At each step of the scan, for an off-axis pixel, at an angle θ , the OPD x_θ with respect to the OPD on-axis x is simply (see e.g. Martin et al. 2016)

$$x_\theta = x \cos(\theta) \quad (29)$$

Table 2. Flux calibration check against various references. Three different filters have been checked: SN1 (362.6–385.6 nm), SN2 (482–513 nm) and SN3 (647.3–685.4 nm).

Object	Wavelength range	Error
NGC3344	$H\alpha$ vs. SpIOMM	-4% \pm 2%
	$H\alpha$ + [NII] λ 6584	-4% \pm 3%
Rousseau-Nepton (2017)		
M1-71 vs. Wright et al. (2005)	$H\alpha$	-7% \pm 3%
	[NII] λ 6584	-11% \pm 3%
NGC628	SN1	-6% \pm 6%
	SN2	-7% \pm 6%
	SN3	-9% \pm 6%
Sanchez et al. (2010)		
HETDEX field (Drissen et al.)	SN2 ($Ly\alpha$ flux of ~ 20 high-redshift galaxies)	-5% \pm 7%
Hill et al. (2008)		

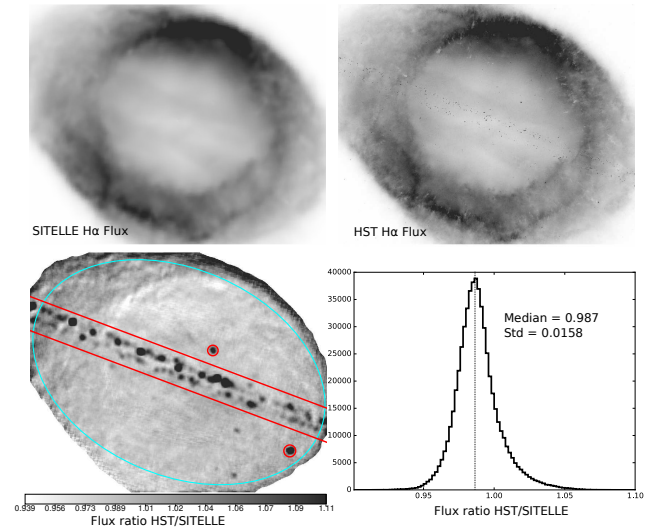


Figure 12. Comparison of the $H\alpha$ flux maps of the planetary nebula M 57 obtained with SITELLE (top-left) and the image obtained through the F656N filter with the Hubble Space Telescope (O'Dell et al. 2013, top-right). The bottom-left quadrant shows the pixel-to-pixel flux ratio and the bottom-right quadrant shows the histogram of the ratios. The HST map has been smoothed with a 8×8 Gaussian kernel to fit SITELLE's pixel scale. The regions shown in red have been excluded from the histogram because they are strong stars and reconstruction errors in the HST mosaic. The region included in the histogram is indicated as a blue ellipse.

If we consider a constant optical step size δ_x^4 , at a given step index j , the on-axis OPD is

$$x = j \delta_x \quad (30)$$

Fourier theorem stands that the maximum wavenumber

⁴ In this paper only optical distances will be considered. The optical distance along the interferometer axis x is roughly 2 times the mechanical position of the scanning mirror. Note also that all distances are always measured with respect to the ZPD.

σ_{\max} that can be measured is inversely proportional to two times the sampling step size.

$$\sigma_{\max,\theta} = \frac{1}{2\delta_x \cos(\theta)} \quad (31)$$

Like its predecessor, SpIOMM, SITELLE's observing mode makes use of spectral folding (Grandmont 2006; Drissen et al. 2010; Grandmont et al. 2012). Because the light is observed through a filter, one can discriminate between all the multiples of a given wavelength that do not fall into the observed passband. It is therefore possible to scan with a sampling step that is a multiple of the minimum observed wavelength and increase the resolution without folding the spectral information. The folding order n of the observation can be related to the number of times the step size is increased:

$$\delta_{x,n} = (n+1)\delta_x. \quad (32)$$

The maximum observable wavenumber, $\sigma_{\max,\theta}$, is then,

$$\sigma_{\max,\theta} = \frac{n+1}{2\delta_x \cos(\theta)}, \quad (33)$$

If we want to make sure that all the wavelengths of the observed light are discriminated by the Fourier transform we must also limit the passband to a minimum wavenumber, $\sigma_{\min,\theta}$,

$$\sigma_{\min,\theta} = \frac{n}{2\delta_x \cos(\theta)} \quad (34)$$

If the spectrum has N samples, the wavenumber associated to a channel i of the output spectrum is

$$\sigma_{i,\theta} = \sigma_{\min,\theta} + \frac{i}{N}(\sigma_{\max,\theta} - \sigma_{\min,\theta}) = \frac{1}{2\delta_x \cos(\theta)} \left(n + \frac{i}{N} \right) \quad (35)$$

We see that, to make an absolute calibration, the value of the incident angle of the light for each pixel of the cube is the only quantity needed. Inversely, if one measures the exact position, in channels, of the centroid of a line with a known wavelength, the incident angle of the spectrum can be derived from equation 35. From equation 35 we can relate directly the wavenumber, σ , of source measured at an angle θ with respect to the axis of the interferometer to its real wavenumber σ_0

$$\sigma = \sigma_0 \cos(\theta). \quad (36)$$

The zero point must therefore be calibrated for each spectrum of the cube via the observation of a laser source at zenith. One source of uncertainty comes from the fact that the deformation of the optical structure when the telescope moves from the Zenith position to the direction of the source has a strong impact on the incident angle seen by one pixel. By comparing calibration maps taken at 47 degrees in 4 directions (north, south, east, west) we have found that this calibration method is likely to produce a gradient in the relative wavelength calibration of up to 15 km s^{-1} . Note that the original wavelength calibration of a cube (especially in the SN3 red filter) can be improved to a precision of a few km s^{-1} by fitting the Meinel OH bands which are generally present everywhere in the cube (see Figure 13 and Figure 14). This operation can be done with ORCS (Martin et al. 2015) and has been used by Martin et al. (2016) and Shara et al. (2016).

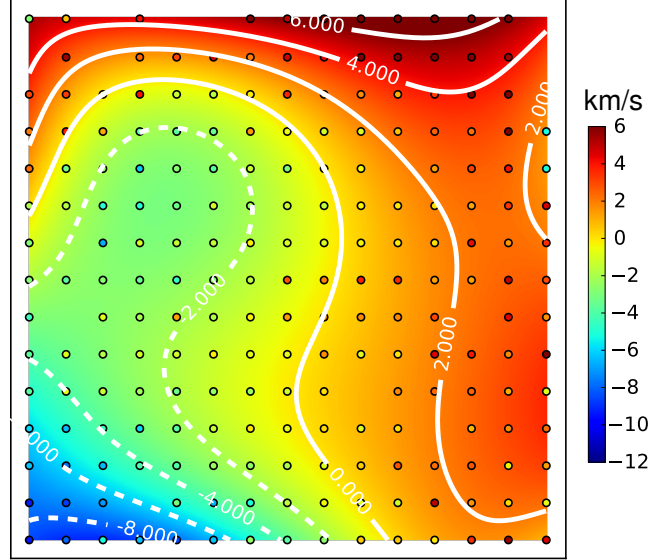


Figure 13. Relative velocity map calculated from sky lines. Extracted from a SN3 cube of PG1216+069 at R=1900 (courtesy of Wei-Hao Wang).

A calibration laser map model has also been developed to increase the precision of the calibration and reconstruct the velocity field in regions where the OH lines are not visible (see Martin et al., in preparation).

The quality of the calibration has been checked by comparing the velocity of 124 planetary nebulae (PNe) detected with SITELLE in M 31, from a low resolution data cube obtained during the commissioning, with the velocity measured by Merrett et al. (2006). 86 of the 124 PNe show a compatible velocity within the uncertainties (see Figure 15). A much more precise checking has been obtained with an intermediate resolution spectral cube of the same region obtained in August 2016 (see Martin et al. in preparation). We have also compared the velocity map of M 57 obtained with SITELLE with the data obtained by O'Dell et al. (2007, 2013) with an Echelle spectrograph (Martin et al. 2016) and found to be in good agreement with an overall precision below 0.5 km s^{-1} on the absolute and relative wavelength calibration.

Another source of absolute calibration uncertainty is the lack of precision on the calibration laser wavelength. The error on the velocity measurement ϵ_v is related to the error on the calibration laser wavelength, ϵ_σ , since

$$\epsilon_v = c \frac{\epsilon_\sigma}{\sigma_{\text{laser}}}, \quad (37)$$

with σ_{laser} the real wavelength of the calibration laser. Therefore, an error of 1 \AA on the calibration laser wavelength translates into an error of 55 km s^{-1} . This bias is easy to correct since the measurement of the Meinel OH bands in a few cubes is enough to obtain a better measurement. For the data release 1 we have used the manufacturer value of 543.5 nm which appears to be biased by $80 \pm 5 \text{ km s}^{-1}$.

6 ASTROMETRIC CALIBRATION

Astrometric calibration is computed from the fit of the point-like sources detected in the field-of-view and the trans-

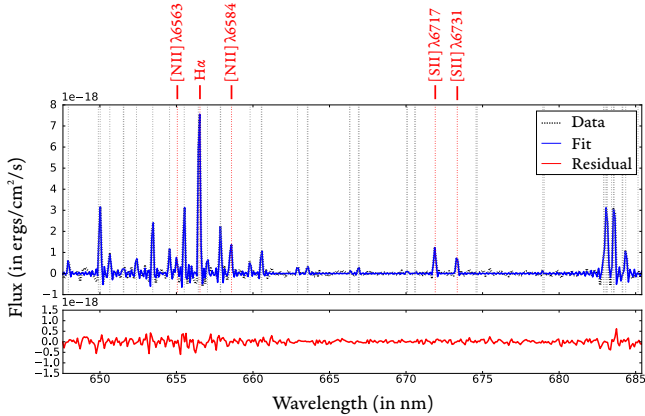


Figure 14. Example of a fit of the Meinel OH bands of a sky spectrum in the field of IC 348. $R = 4500$ (courtesy of Gregory Herczeg). The fitted emission lines of the diffuse gas around the nebula are shown.

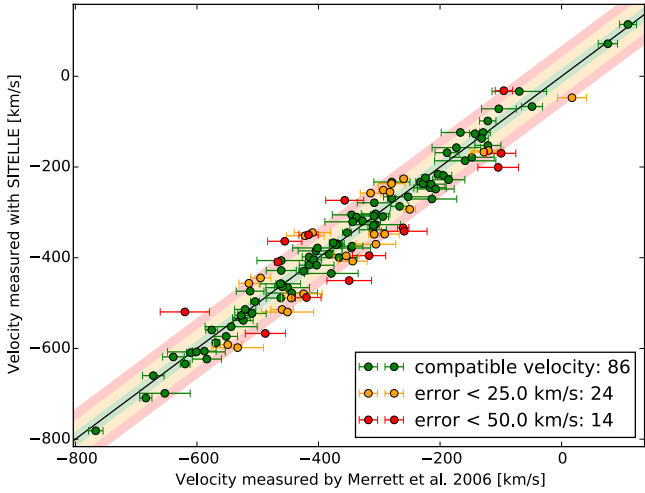


Figure 15. Comparison of the measured velocity of 124 planetary nebulae detected with SITELLE in M31 with the measurement of Merrett et al. (2006). The resolution of the cube is 400. The one-to-one line is indicated by a black line.

formation of their celestial coordinates (Greisen & Calabretta 2002) found in the USNO-B1 catalog (Monet et al. 2003). The quality and the number of sources of the more recent Gaia data release 1 catalog has motivated its use for the next release instead of the old USNO catalog (Gaia Collaboration 2016). The fitting engine fits all the stars at the same time which enhances the precision of the transformation parameters. The astrometric calibration is limited to 3 pixels ($\sim 1''$) in an 11 arc-minutes circle around the center of the field by the optical distortions which are not taken into account in the present data release (see Figure 16).

7 CONCLUSIONS

We have discussed the calibration quality of SITELLE’s first data release. We have shown that the absolute flux calibration was biased by -5% and that it was subject to a 5% vari-

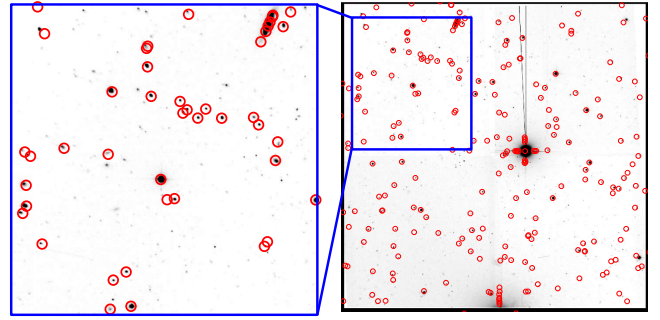


Figure 16. Positions of the stars from the USNO-B1 catalog transformed with the computed World Coordinate System (WCS) of the field around the planetary nebula M1-71.

ability from one observation to another. The general bias is likely to be corrected in the next release via a more precise evaluation of the modulation efficiency. But this results must be tempered with the fact that major flux calibration biases cannot be avoided. We thus recommend that the flux calibration be checked against external data. A $\sim 2\%$ pixel-to-pixel error is expected on the basis of a comparison with an Hubble images of M 57. The absolute wavelength calibration is also biased by $80 \pm 5 \text{ km s}^{-1}$ due to the lack of precision on the calibration laser wavelength. The pixel-to-pixel error on the calibration can be as large as 15 km s^{-1} but it can be easily corrected by measuring the velocity of Meinel OH bands in the cube. This operation can be done with ORCS (Martin et al. 2015). The astrometric calibration is done via the comparison with the USNO-B1 catalog and is limited to $\sim 1''$ by the optical distortions which are not corrected in the present release. All the observed biases will be corrected in the next release. The precision on the pixel-to-pixel wavelength calibration will also be enhanced by the analysis of the internal phase of each cube that is directly related to the angle of the incident light and therefore to the velocity calibration (Martin et al., in preparation). The precision of the pixel-to-pixel flux calibration will also be enhanced by using a 3D phase correction and a better flatfield correction.

ACKNOWLEDGEMENTS

This paper is based on observations obtained with SITELLE, a joint project of Université Laval, ABB, Université de Montréal and the Canada-France-Hawaii Telescope (CFHT) which is operated by the National Research Council (NRC) of Canada, the Institut National des Science de l’Univers of the Centre National de la Recherche Scientifique (CNRS) of France, and the University of Hawaii. LD is grateful to the Natural Sciences and Engineering Research Council of Canada, the Fonds de Recherche du Québec, and the Canadian Foundation for Innovation for funding.

REFERENCES

Baril M. R., et al., 2016, in Evans C. J., Simard L., Takami H., eds, Proceedings of SPIE. International Society for Optics and Photonics, p. 990829, doi:10.1117/12.2232075

- Bell R. J., 1972, *Introductory Fourier Transform Spectroscopy*. Academic Press, New York, New York, USA
- Bernier A.-P., 2006, in *Proceedings of SPIE*. SPIE, pp 626949–626949–9, doi:10.1117/12.671410
- Buton C., et al., 2012, *Astronomy & Astrophysics*, 549, A8
- Davis S. P., Abrams M. C., Brault J. W. J. W., 2001, *Fourier transform spectrometry*. Academic Press, San Diego
- Doug T., 1993, in Hanisch R. J., Brissenden R. J. V., Barnes J., eds, Vol. 52, *Astronomical Data Analysis Software and Systems II*. Astronomical Society of the Pacific, p. 173
- Drissen L., Bernier A.-P., Rousseau-Nepton L., Alarie A., Robert C., Joncas G., Thibault S., Grandmont F., 2010, in McLean I. S., Ramsay S. K., Takami H., eds, Vol. 7735, *SPIE Astronomical Telescopes + Instrumentation*. International Society for Optics and Photonics, pp 77350B–77350B–10, doi:10.1117/12.856470
- Gaia Collaboration G., 2016, eprint arXiv:1609.04153
- Grandmont F., 2003, in *Proceedings of SPIE*. SPIE, pp 392–401, doi:10.1117/12.457339
- Grandmont F., 2006, PhD thesis, Université Laval
- Grandmont F., Drissen L., Mandar J., Thibault S., Baril M. R., 2012, in McLean I. S., Ramsay S. K., Takami H., eds, Vol. 8446, *SPIE - Ground-based and Airborne Instrumentation for Astronomy IV*. International Society for Optics and Photonics, p. 84460U, doi:10.1117/12.926782
- Greisen E. W., Calabretta M. R., 2002, *Astronomy and Astrophysics*, 395, 1061
- Hill G. J., et al., 2008, in Kodama T., Toru Y., Aoki K., eds, *ASP Conference Series Vol. 399, Panoramic Views of Galaxy Formation and Evolution*. Astronomical Society of the Pacific, p. 115
- Kelz A., et al., 2006, *Publications of the Astronomical Society of the Pacific*, 118, 129
- Learner R. C. M., Thorne A. P., Wynne-Jones I., Brault J. W., Abrams M. C., 1995, *Journal of the Optical Society of America A*, 12, 2165
- Maillard J. P., Drissen L., Grandmont F., Thibault S., 2013, *Experimental Astronomy*, 35, 527
- Martin T., 2015, Phd thesis, Université Laval
- Martin T., Drissen L., 2016, in Reylé C., Richard J., Cambrésy L., Deleuil M., Pécontal E., Tresse L., Vauglin I., eds, *Proceedings of the annual meeting of the French Society of Astronomy & Astrophysics Lyon, June 14-17, 2016*. No. October in *Proceedings of the annual meeting of the French Society of Astronomy & Astrophysics*. pp 23–28
- Martin T., Drissen L., Joncas G., 2012, in Radziwill N. M., Chiozzi G., eds, Vol. 2, *SPIE - Software and Cyberinfrastructure for Astronomy II*. pp 84513K–84513K–9, doi:10.1117/12.925420
- Martin T., Drissen L., Joncas G., 2015, *Astronomical Data Analysis Software and Systems XXIV (ADASS XXIV)*, 495
- Martin T. B., Prunet S., Drissen L., 2016, eprint arXiv:1608.05854
- Merrett H. R., et al., 2006, *Monthly Notices of the Royal Astronomical Society, Volume 369, Issue 1*, pp. 120-142., 369, 120
- Monet D. G., et al., 2003, *The Astronomical Journal*, 125, 984
- O'Dell C. R., Sabbadin F., Henney W. J., 2007, *The Astronomical Journal*, 134, 1679
- O'Dell C. R., Ferland G. J., Henney W. J., Peimbert M., 2013, *The Astronomical Journal*, 145, 92
- Rousseau-Nepton L., 2017, PhD thesis, Université Laval
- Sakai H., Vanasse G. A., Forman M. L., 1968, *Journal of the Optical Society of America*, 58, 84
- Sanchez S. F., Rosales-Ortega F. F., Kennicutt R. C., Johnson B. D., Diaz A. I., Pasquali A., Hao C. N., 2010, *Monthly Notices of the Royal Astronomical Society, Volume 410, Issue 1*, pp. 313-340., 410, 313
- Shara M. M., Drissen L., Martin T., Alarie A., Stephenson F. R., 2016, *Monthly Notices of the Royal Astronomical Society*, 465, 739
- Wright S. a., Corradi R. L. M., Perinotto M., 2005, *Astronomy and Astrophysics*, 436, 9

This paper has been typeset from a $\text{\TeX}/\text{\LaTeX}$ file prepared by the author.